

1 **Illuminating a Contorted Slab with a Complex Intraslab**  
2 **Rupture Evolution during the 2021  $M_W$  7.3 East Cape, New**  
3 **Zealand Earthquake**

4 **Ryo Okuwaki<sup>1,2,3,=</sup>, Stephen P. Hicks<sup>4, =</sup>, Timothy J. Craig<sup>3</sup>, Wenyan Fan<sup>5</sup>, Saskia**  
5 **Goes<sup>4</sup>, Tim J. Wright<sup>3</sup>, and Yuji Yagi<sup>2</sup>**

6 <sup>1</sup>Mountain Science Center, University of Tsukuba, Tsukuba, Ibaraki 305-8572, Japan

7 <sup>2</sup>Faculty of Life and Environmental Sciences, University of Tsukuba, Tsukuba, Ibaraki 305-8572, Japan

8 <sup>3</sup>COMET, School of Earth and Environment, University of Leeds, Leeds LS2 9JT, UK

9 <sup>4</sup>Department of Earth Science and Engineering, Imperial College London, London SW7 2AZ, UK

10 <sup>5</sup>Scripps Institution of Oceanography, UC San Diego, La Jolla, California 92093, USA

11 **Key Points:**

- 12 • A moment magnitude 7.3 2021 East Cape, New Zealand intraslab earthquake  
13 comprised multiple rupture episodes with different faulting styles  
14 • The complex rupture comprises components of shallow trench-normal exten-  
15 sion and unexpectedly, deep trench-parallel compression in slab  
16 • The trench-parallel compression likely reflects stress rotation at a buoyancy con-  
17 trast that drives slab contortion

---

<sup>=</sup>Equally contributing author

Corresponding author: Ryo Okuwaki, rokuwaki@geol.tsukuba.ac.jp

18 **Abstract**

19 The state-of-stress within subducting oceanic plates controls rupture processes of deep  
20 intraslab earthquakes. However, little is known about how the large-scale plate ge-  
21 ometry and the stress regime relate to the physical nature of the deep-intraslab earth-  
22 quakes. Here we find, by using globally and locally observed seismic records, that the  
23 moment magnitude 7.3 2021 East Cape, New Zealand earthquake was driven by a com-  
24 bination of shallow trench-normal extension and unexpectedly, deep trench-parallel  
25 compression. We find multiple rupture episodes comprising a mixture of reverse, strike-  
26 slip, and normal faulting. Reverse faulting due to the trench-parallel compression is  
27 unexpected given the apparent subduction direction, so we require a differential-buoyancy  
28 driven stress rotation which contorts the slab near the edge of the Hikurangi plateau.  
29 Our finding highlights that buoyant features in subducting plates may cause diverse  
30 rupture behavior of intraslab earthquakes due to the resulting heterogeneous stress  
31 state within slabs.

32 **Plain Language Summary**

33 A key type of tectonic boundary is where two plates collide with one sinking into the  
34 mantle beneath. These subduction zones generate the world's largest earthquakes. Quan-  
35 tifying stress in the subducting plate ("slab") is important because slabs drive the global  
36 plate-tectonic system, and large earthquakes can occur within them. These earthquakes  
37 can cause strong shaking, and, when occurring near cities, can lead to damage. How-  
38 ever, mapping stress is challenging as we cannot directly "see" inside deep slabs. Our  
39 best indications of slab stress come from earthquakes themselves. A magnitude 7.3  
40 earthquake north of New Zealand in 2021 generated a distinct pattern of seismic wave-  
41 forms at seismometers installed worldwide. We used these seismic records to probe  
42 the earthquake, providing a new view of stress in subduction zones. We found the earth-  
43 quake generated both vertical and horizontal motions along faults, driven by compres-  
44 sional and extensional stresses deep within the slab. The compressional part is ori-  
45 ented 90 degrees from the subduction direction, which is opposite to the usual com-  
46 pression in subduction zones, and has not been observed before. This unusual direc-  
47 tion of compression can be explained by subduction of a thickened and buoyant part  
48 of the Pacific plate, known as the Hikurangi plateau.

## 1 Introduction

Complex fault configurations and heterogeneous fault conditions, i.e., stress and strength states, govern earthquake rupture development and propagation (Avouac et al., 2014; Floyd et al., 2016; Elliott et al., 2016; Hamling et al., 2017). Such relations can be inferred from the fault geometry and long-term geodetic observations for shallow active faults (Simons et al., 2002; Williams et al., 2013; Elliott et al., 2016; Arai et al., 2016; Hamling et al., 2017; Hayes et al., 2018; Sippl et al., 2018). However, for intraslab earthquakes occurring below  $\sim 50$  km depth, these physical controlling factors are difficult to assess because of challenges to map structure at such depths, and the general lack of seismicity there (Wiens, 2001; Ranero et al., 2005; Page et al., 2016; Dascher-Cousineau et al., 2020; Gomberg & Bodin, 2021). In particular, the internal stress state and its extensional-compression transition regime are often elusive in subducted slabs, although they directly impact intraslab earthquake occurrence and their faulting styles (Astiz et al., 1988; Ammon et al., 2008; Craig et al., 2014; Romeo & Álvarez-Gómez, 2018; Sandiford et al., 2019, 2020; Ye et al., 2021). Thus, imaging the rupture processes of large, deep intraslab earthquakes offers a rare window to investigate the slab configuration, and to understand fault interaction and rupture evolution of these earthquakes, illuminating heterogeneous stress fields.

An intraslab moment magnitude ( $M_W$ ) 7.3 earthquake occurred offshore the East Cape in northern New Zealand on 4th March 2021, which was followed  $\sim 4$  hours later by a series of the  $M_W$  7.4 and  $M_W$  8.1 earthquakes in the Kermadecs ( $\sim 900$  km to the north) (GeoNet, 2021). The  $M_W$  7.3 2021 East Cape earthquake, which is the focus of this paper, may offer insight into the regional slab geometry because of its location and complex rupture process. The 2021 East Cape earthquake locates at the boundary between the southern end of Kermadec trench and the northern end of Hikurangi margin, where the Pacific plate subducts beneath the Australian plate and its convergence decreases and progressively rotates to oblique motion toward the south (Fig. 1) (Collot et al., 1996, 2001; Lewis et al., 1998; Wallace et al., 2009). The reported centroid depth of the earthquake was  $\sim 50$  km (U.S. Geological Survey Earthquake Hazards Program, 2017; Duputel et al., 2012; Dziewonski et al., 1981; Ekström et al., 2012), and the focal mechanism indicates oblique-thrust motion, with the principal stress axis oriented towards the north-south direction (Fig. 1) (U.S. Geological Survey Earthquake Hazards Program, 2017; Duputel et al., 2012; Dziewonski et al., 1981; Ekström et al., 2012). This stress axis suggests the earthquake was not a simple shallow normal- or reverse-faulting event with the strike angle oriented parallel to the trench axis, as is typically seen in many subduction zones (Fig. 1) (U.S. Geological Survey Earthquake

85 Hazards Program, 2017; Duputel et al., 2012; Dziewonski et al., 1981; Ekström et al.,  
86 2012). However, the earthquake produced observable tsunami signals at tide gauges  
87 at the northern coast of New Zealand (GeoNet News, 2021), indicating seafloor de-  
88 formation due to possible shallow slip. All these apparently inconsistent observations  
89 (GeoNet, 2021; GeoNet News, 2021) suggest a complex rupture process of the East  
90 Cape earthquake, possibly involving multiple faults at different depths.

91 Although the subduction-related deformation processes in the southern part of  
92 the Hikurangi subduction zone have received a lot of scientific attention (e.g., Wal-  
93 lace et al., 2009; Nishikawa et al., 2021), the northern segment of Hikurangi margin,  
94 where it transitions to the Tonga-Kermadec arc, is less well understood. In the East  
95 Cape region, sporadic deep seismicity (>80-km depth) contrasts with abundant shal-  
96 low seismicity (<50-km depth) (Dziewonski et al., 1981; Ekström et al., 2012; GeoNet  
97 Moment Tensors, 2021; U.S. Geological Survey Earthquake Hazards Program, 2017;  
98 GeoNet, 2021). Most of the shallow earthquakes are normal faulting events within the  
99 top of the oceanic plate due to trench-normal extensional stress due to slab bending  
100 into the trench (Reyners & McGinty, 1999; Henrys et al., 2006; Bassett et al., 2010).  
101 With these shallow earthquakes, the plate interface and the surrounding materials have  
102 been imaged down to ~20 km depth (Davey et al., 1997; Bell et al., 2010; Bassett et  
103 al., 2010, 2016), but the lithospheric structure of the deep slab is poorly resolved. The  
104 apparent complex rupture process of the 2021 East Cape earthquake offers a unique  
105 opportunity to image the stress regime associated with the deeper subduction pro-  
106 cess.

107 Here we show that the rupture process of the 2021 East Cape earthquake involves  
108 multiple rupture episodes with a mixture of reverse, strike-slip, and normal faulting  
109 mechanisms. These episodes ruptured multiple faults through the subducted oceanic  
110 lithosphere at various depths. The earthquake initiated at 70 km depth with an un-  
111 expected trench-parallel compressional reverse faulting mechanism, and followed by  
112 a slip episode at 30 km depth, which is likely governed by more usual slab-bending  
113 trench-normal down-dip extensional stresses. Such a rupture process reflects a het-  
114 erogeneous stress regime within the subducted slab, in response to a possible geomet-  
115 ric change of the slab in depth due to either the subduction of a seamount associated  
116 with the Ruatoria debris slide (Lewis et al., 1998; Collot et al., 2001; Lewis et al., 2004),  
117 or a sharp change in slab buoyancy at the northern end of the subducting Hikurangi  
118 oceanic plateau.

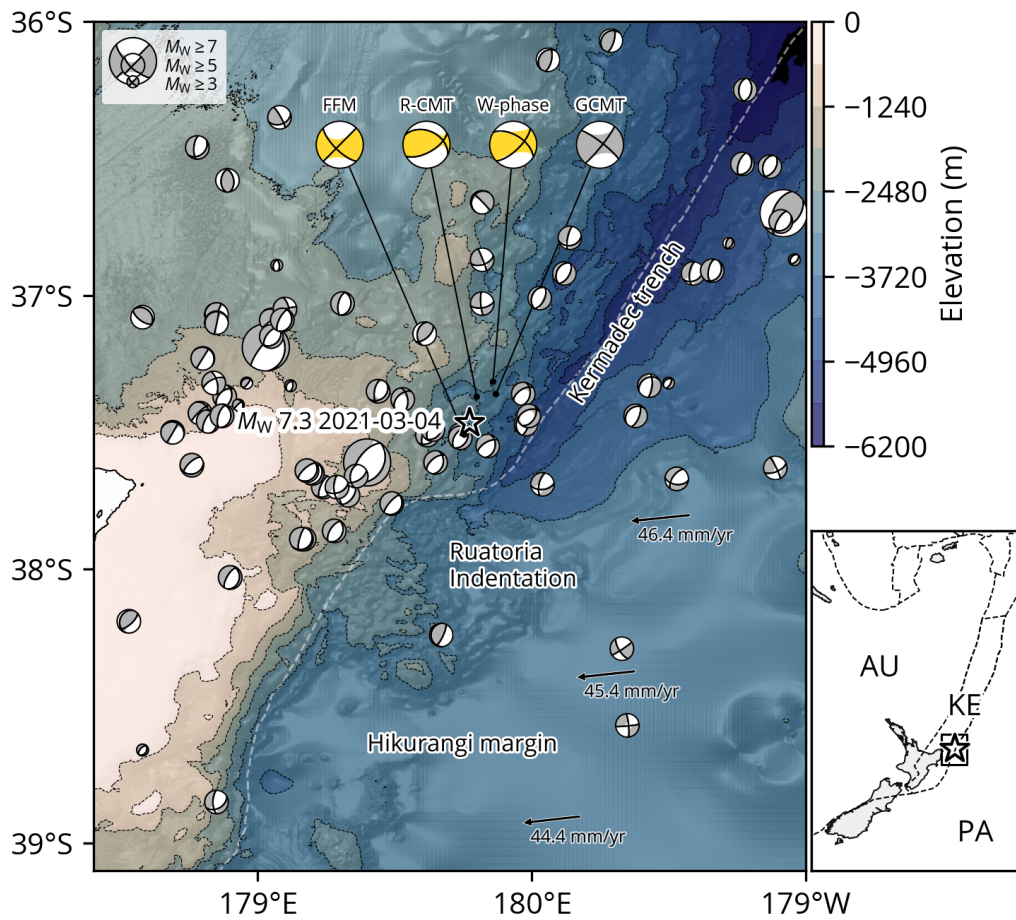


**Figure 1.** Seismo-tectonic overview of the study region in the East Cape, New Zealand. The star shows the relocated hypocenter of the  $M_w$  7.3 2021 East Cape earthquake. Gray beach balls are the lower-hemisphere stereographic projection of the moment tensor solutions before the 2021 East Cape earthquake (Dziewonski et al., 1981; Ekström et al., 2012). Yellow beach balls are the moment tensor solutions for the 2021 East Cape earthquake obtained by this study (FFM; Finite-fault model, R-CMT; regional centroid moment tensor, W-phase; W-phase moment tensor). Background contours display the bathymetry (Mitchell et al., 2012). The arrows show the relative plate motions with the convergence rate of the Pacific plate (PA) towards the fixed Australian plate (AU) (DeMets et al., 2010). The dashed line gives the approximate location of the subduction trench (e.g., Bassett et al., 2010). The right map shows the wider setting of the study region. The rectangle shows the area of the left map. The star marks the epicenter. The dashed lines are the plate boundaries (Bird, 2003) between the Pacific (PA), the Australian (AU) and the Kermadec (KE) plates.

## 119 2 Hypocenter, aftershock relocation, and initial source estimates

120 We first determined the hypocenter of the East Cape earthquake by non-linear  
121 inversion of  $P$ - and  $S$ -wave arrival times at regional distances using a 1D velocity model  
122 appropriate for the East Cape region (Text S1; Fig. S1). Our relocated epicenter lies  
123 along the trench axis, and is within 10 km of the GeoNet solution (GeoNet, 2021), and  
124  $\sim 35$  km ENE of the U.S. Geological Survey National Earthquake Information Center  
125 (USGS-NEIC) solution (U.S. Geological Survey Earthquake Hazards Program, 2017)  
126 which is consistent with the USGS-NEIC epicenters being systematically shifted to the  
127 down-dip direction in subduction zones (e.g., Ye et al., 2017). Our maximum-likelihood  
128 hypocenter depth is 72 km. Although this hypocenter depth may be thought to be in-  
129 herently uncertain due to the sub-optimal station coverage, it provides an initial hy-  
130 pothesis for testing our results of the more complex rupture configuration later. If we  
131 instead fix our hypocentral depth at the fixed GeoNet/USGS estimates of 10–12 km  
132 (GeoNet, 2021; U.S. Geological Survey Earthquake Hazards Program, 2017), the root-  
133 mean-square residual of arrival times at the closest stations ( $< 200$  km) increases by  
134 0.3 s, suggesting that a shallow depth is less compatible with the observations. How-  
135 ever, no depth phases were reported in the International Seismological Centre Bul-  
136 letin for this earthquake (International Seismological Centre, 2021), presumably due  
137 to interference with the long source-time function.

138 Next, we used the COMLOC package (Lin & Shearer, 2005, 2006) to relocate earth-  
139 quakes near the mainshock hypocenter. The algorithm uses the source-specific sta-  
140 tion term (SSST) method to relocate the earthquakes, which can greatly improve the  
141 relative locations of nearby events because of implementing empirical corrections to  
142 neutralize the 3D velocity effects (Richards-Dinger & Shearer, 2000; Lin & Shearer,  
143 2005). We focus on events occurring from January 1, 2021 to May 1, 2021 near the  
144 source region of the 2021 East Cape earthquake as there were few events in the re-  
145 gion prior to the earthquake. These events are relocated using both  $P$ - and  $S$ -wave phase  
146 picks from GeoNet (2021) and a 1D velocity profile taken from the NZW2.2 model  
147 (Eberhart-Phillips et al., 2010, 2020). We selected the L1-norm as the traveltimes-residual  
148 misfit measure, and obtained locations for 3484 events (Fig. S2). We find that the dis-  
149 tribution of aftershocks from one week after the mainshock (1556 events) is spread  
150 across the whole lithosphere, from the seafloor down to  $\sim 100$  km in depth. In par-  
151 ticular, the deep aftershocks corroborate our deep mainshock hypocenter hypothesis,  
152 and the aftershock distribution indicates a possible multi-fault rupture process of the  
153 East Cape earthquake.

154 Using a Bayesian bootstrapping centroid-moment tensor (CMT) inversion of low-  
155 frequency (2.0–8.5 mHz) teleseismic waveforms for a single-point source (Text S2),  
156 we find a mean centroid depth of 53 km, with a centroid position shifted 18 km NNE  
157 of the epicenter, and time shift from the origin time of +5 s (Fig. S3). However, the  
158 CMT solution has a large non-double couple component (DC=15%). Such a low DC  
159 component is likely caused by geometric complexities of the earthquake that may in-  
160 volve multiple faults within the subducted Pacific plate near the Hikurangi trench.

161 Finally, to test the hypothesised rupture complexity, we investigated the rupture  
162 process of the earthquake with a multi-point centroid moment tensor (R-CMT) inver-  
163 sion method using regional seismic waveforms (Text S3; Figs. S4 to S6). The approach  
164 can resolve the first-order features of a complex rupture with few assumptions. Due  
165 to the low-velocity accretionary wedge, the later part of the <25 s period surface waves  
166 on the horizontal components at stations within ~400 km epicentral distance are poorly  
167 fit (Figs. S5 and S6) due to basin resonance effects (Kaneko et al., 2019). We find that  
168 the East Cape event can be best explained by two sub-events, with the largest sub-  
169 event ( $M_W \sim 7.3$ ) at 50–70 km depth occurring 8–10 s after the origin time, and the  
170 second sub-event at 7–12 km depth and 6–8 s after the first sub-event. The second  
171 sub-event significantly increases waveform variance reduction by 16–23%. The first  
172 sub-event has an oblique-reverse mechanism. Given the inclination of the deep after-  
173 shocks near the hypocenter (Fig. S2), the fault plane is possibly dipping north and strik-  
174 ing along the east-west faulting plane. Conversely, the second sub-event has a normal  
175 faulting mechanism. The shallow aftershock lineation (10–30 km depth) dips to the  
176 west (Fig. S2), which suggests the fault plane is likely oriented along the trench axis.  
177 Overall, our R-CMT solution corroborates a complex rupture scenario involving at least  
178 two sub-events separated by ~40 km in depth: one in the top of the Pacific plate, the  
179 other deep within the slab.

### 180 **3 Intermittent complex multiple rupture episodes with various focal mechanisms**

181 To better understand the rupture development, we applied a finite-fault potency-  
182 density inversion method (Shimizu et al., 2020) to estimate the slip evolution of the  
183 2021 East Cape earthquake (Text S4). The method can flexibly accommodate multi-  
184 ple faults with different geometries rupturing during the same event, which are in-  
185 ferred from the spatiotemporal distribution of five-basis double-couple components  
186 of the potency-density tensors (Kikuchi & Kanamori, 1991; Ampuero & Dahlen, 2005).  
187 The method has proven effective at resolving complex earthquake ruptures in a va-  
188 riety of tectonic settings (Shimizu et al., 2020, 2021; Okuwaki et al., 2020; Tadapan-

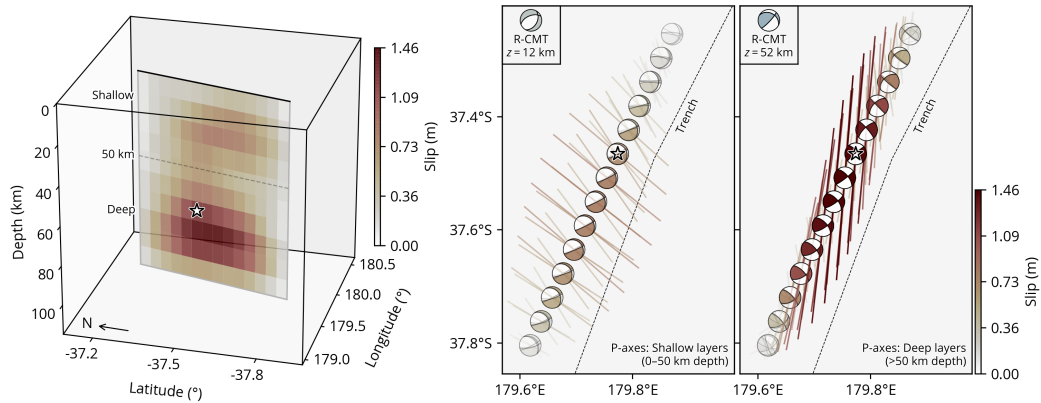


**Figure 2.** Static slip distribution. The left panel shows the total slip distribution in a 3D view, viewed from the south-west. The star represents our hypocenter. The black line shows the top of the model fault. The right panels show the map view of the slip distribution from shallow (<50 km) and deep depths ( $\geq 50$  km), with beach balls representing double-couple components (Fig. S7), and corresponding P-axis azimuths (bars scaled by slip). The P-axis azimuth is extracted from the resultant double-couple solution for each sub-fault, which is represented by a lower-hemisphere stereographic projection. We show the beach balls from the slip patch corresponding to the fault element with the maximum slip within each given depth range. The inset shows the corresponding R-CMT solutions annotated with their depths ( $z$ ). The dashed line is the subduction trench (Bird, 2003).



189 sawut et al., 2021; Yamashita et al., 2021). In practice, we parametrize a 2D vertical  
190 model domain along a 200° strike extending from 7- to 107-km depth with a total of  
191 140 source elements (sub-faults) (Fig. 2). This parameterization is guided by the ob-  
192 served cluster of the near-trench-parallel aftershocks (Fig. S2). In the 2D model do-  
193 main, we solve the fault-normal and shear-slip vectors at each source element, which  
194 are independent of the model domain geometry. In other words, we solve distributed  
195 sources in the model domain that may have any types of faulting mechanism required  
196 by the data. The model domain therefore allows multiple faulting episodes of the earth-  
197 quake and does not necessarily indicate a single fault plane cutting through the litho-  
198 sphere a continuous rupture. Our preferred slip model suggests that the earthquake  
199 initiated at 72 km depth (Fig. S12) corroborating the relocated hypocenter and the R-  
200 CMT solution.

201 Our preferred finite-fault model suggests that most slip occurred at 55 to 100  
202 km depth and ~15 km south of the hypocenter, releasing 69% of the total moment  
203 (Fig. 2). Another patch of slip is observed at 20–40 km depth, much shallower than  
204 the hypocentral depth and comprising 31% of the total moment. The deeper slip is  
205 dominated by an oblique strike-slip faulting mechanism. The shallow slip involves  
206 a mixture of normal and strike-slip faulting mechanisms. The finite-fault model leads  
207 to a moment estimate of  $1.7 \times 10^{20}$  Nm ( $M_W$  7.4).

208 The rupture process of the East Cape earthquake involved at least four distinct  
209 episodes (E1 to E4) with the deep- and shallow-slips corresponding to different fault-  
210 ing types. The earthquake initiated as a reverse faulting with a strike-slip component  
211 for the first 5 s (E1, Fig. 3). The rupture then propagated towards the south at 60–  
212 100 km depth, releasing 20% of the total moment and lasting for about 5 s (E2, Fig.  
213 3). This episode was dominated by thrust faulting. The third episode (E3) simulta-  
214 neously ruptured several fault patches from 10 to 15 s, including a shallow patch at  
215 ~25 km depth and a deep patch ~70 km depth (Fig. 3). The shallow part of E3 rup-  
216 tured with a normal faulting mechanism, while the deep patch of E3 had a strike-slip  
217 mechanism. The last major episode (E4) ruptured a fault patch beneath the hypocen-  
218 ter for about 5 s with a dominant strike slip focal mechanism (Fig. 3). The remain-  
219 ing 26% of the total moment was released by slips at both shallow and deep regions,  
220 and the earthquake lasted for about ~30 s.

221 The four rupture episodes are compact in size and are spatially distinct from each  
222 other. Given the varying focal mechanisms, the chaotic episodes likely do not result  
223 from the same continuous rupture front, but more likely represent segmented slip on  
224 different faults that may have interacted with, and triggered, each other.

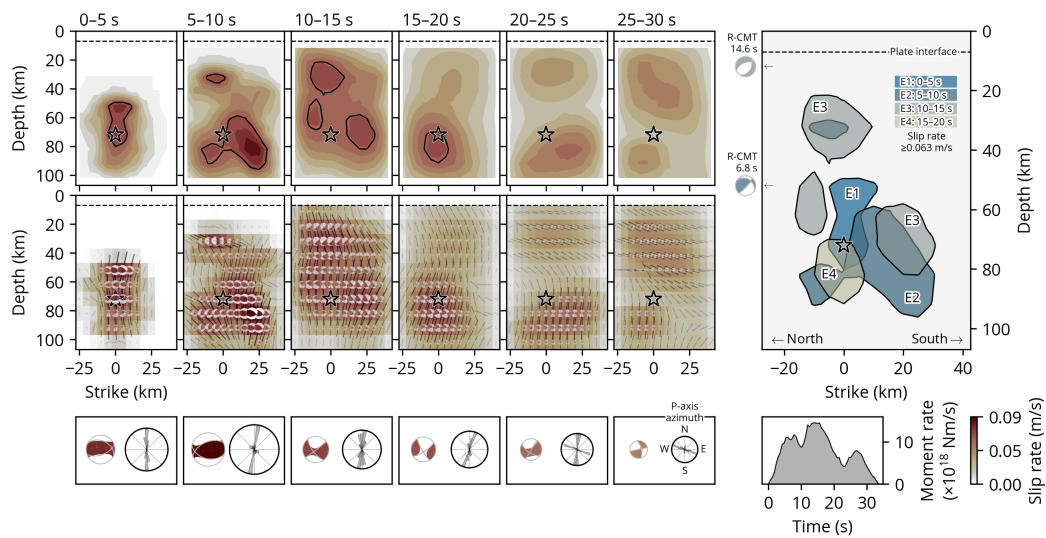


**Figure 3.** Slip evolution. The left panels show the cross sections of the spatio-temporal distribution of slip rate and the resultant moment-rate tensor solution, given in 5 s long windows. The star represents the hypocenter. The dashed line is the top of the subducting plate (Bassett et al., 2010). The black contour highlights faster slip rates ( $\geq 0.063$  m/s;  $\geq 70\%$  of maximum slip rate). The centroid moment tensor for each time window is shown at the bottom, together with the rose diagram of P-axis azimuths weighted by slip rate. All the beach balls of the moment-tensor solution are represented as a lower-hemisphere stereographic projection, not rotated according to the model geometry, but in map view. The right panel summarizes the slip-rate evolution. The color for each episode (E1 to E4) corresponds to the time window. The minor slip-rate events within the final two time windows (20–30 s) are not slipping fast enough to plot a contour on the right panel. R-CMT solutions are also shown at the corresponding depths, with their time shift given relative to the hypocentral time. The right-bottom inset is the total moment-rate function from the finite-fault model.

#### 4 Intralab stress rotation in depth

The source process of the 2021 East Cape earthquake is characterized by spatiotemporally disconnected, multiple episodes rupturing from deep to shallow within the subducted slab. For the shallow slip episode, its focal mechanism shows a mixture of the normal faulting with a strike-slip component. The general trend of the aftershock distribution (Fig. S2) suggests that the fault plane striking toward the northeast-southwest direction likely ruptured during the later phase of the earthquake. It is noteworthy that some aftershocks (U.S. Geological Survey Earthquake Hazards Program, 2017; Dziewonski et al., 1981; Ekström et al., 2012; GeoNet Moment Tensors, 2021) share similar focal mechanisms to the shallow rupture episode (Fig. S8). Given the near-trench location of the East Cape earthquake, there is some ambiguity regarding the exact faulting configuration. However, the aftershock distribution indicates that the shallow slip episode likely ruptured a normal fault within the downgoing plate. Additionally, in the absence of clear shallow slip with a reverse-faulting mechanism, this normal faulting episode likely caused the observed tsunami.

The varying focal-mechanisms of the four slip episodes (E1–E4) show the compressional stress orientation (the P-axis orientation) of the East Cape earthquake rotated from the northwest-southeast direction to the north-south direction with a gap in slip and approximate stress transition depth at ~50 km (Figs. 2 and 3). The normal faulting of the shallow slip episodes striking toward the northeast-southwest direction agrees well with the extensional stress in the upper part of the subducted plate due to the expected plate bending and pulling process (e.g., Astiz et al., 1988; Ammon et al., 2008; Craig et al., 2014; Romeo & Álvarez-Gómez, 2018; Sandiford et al., 2020). Such a bending process seems to have caused most of the background seismicity in this region, which has predominant normal faulting mechanisms (Fig. 1; Reyners & McGinty, 1999; Bassett et al., 2010). If the deep slip at 50–100-km depth during the East Cape earthquake was driven by the same bending-related process, we would expect a trench-normal P-axis orientation, which is typical for similar events at other subduction zones, where deep trench-parallel reverse faulting is observed (e.g., Okada & Hasegawa, 2003; Ohta et al., 2011; Ye et al., 2012; Todd & Lay, 2013; Ye et al., 2021). However, the deep slip patches of the East Cape earthquake (E1 and E2, and R-CMT Sub-event 1) have oblique-thrusting mechanisms, resulting in a trench-parallel compression. This perplexing P-axis orientation indicates an additional regional factor that may have modulated the rupture process of the East Cape earthquake.

The interactivity between various faulting episodes is a puzzling part of the East Cape earthquake. Subduction zone earthquakes may involve multiple disconnected

261 subevents with different faulting types that can trigger and interact with each other  
262 (Ammon et al., 2008; Lay et al., 2013; Hicks & Rietbrock, 2015; Lay et al., 2020). For  
263 the East Cape earthquake, our preferred finite-fault model does not show a contin-  
264 uous rupturing path from the deep to shallow episodes (Figs. 2 and 3). The shallow  
265 rupture E3 is separated by  $\sim 40$  km from the deep episodes and started  $\sim 5$  s later (Fig.  
266 3), suggesting an apparent rupture speed of  $\sim 8$  km/s if the rupture was continuous.  
267 Such a rupture speed would be close to the local  $P$ -wave speed (Table S1), which is  
268 unlikely. More likely, slip episodes E1 and E2 triggered the following shallow episode  
269 E3 due to either the static and/or dynamic stress change from the initial deep rup-  
270 ture. Additionally, the aftershock distribution (Fig. S2) shows a gap at  $\sim 50$ -km depth  
271 in-between the deep and shallow rupture episodes, which may reflect the neutral stress  
272 transition between the shallow extension and deep compression. A stress transition  
273 or strength contrast within the slab can work as an inhomogeneous barrier (Das & Aki,  
274 1977; Aki, 1979) to smooth propagation from deep to shallow rupture during the East  
275 Cape earthquake. Therefore, the rupture evolution of the earthquake may have de-  
276 veloped as discontinuous jumps by means of stress triggering (Miyazawa & Mori, 2005;  
277 Sleep & Ma, 2008; Fischer, Sammis, et al., 2008; Fischer, Peng, & Sammis, 2008) across  
278 the apparent stress/strength barrier between the deep and shallow rupture areas.

279 Large intraplate earthquakes within the downgoing plate in subduction zones  
280 are typically caused either by the down-dip bending and unbending of the slab (e.g.,  
281 Astiz et al., 1988; Craig et al., 2014; Sandiford et al., 2020), the reactivation of ma-  
282 jor oceanic fabrics, including fracture zones (e.g., Abercrombie et al., 2003; Meng et  
283 al., 2012; Yue et al., 2012), or the tearing of the slab (e.g., Tanioka et al., 1995). How-  
284 ever, the orientation and rupture complexity of the 2021 East Cape event deviates from  
285 these typical events. Two events with apparently similar deep trench-parallel com-  
286 pression in the slab include 2003  $M_W$  7.9 Enggano and 2009  $M_W$  7.6 Padang earth-  
287 quakes, offshore Sumatra (Abercrombie et al., 2003; Wiseman et al., 2012). However,  
288 these events likely ruptured pre-existing fabrics in the downgoing plate (Abercrombie  
289 et al., 2003), such as fracture zones (Wiseman et al., 2012). Both earthquakes poten-  
290 tially represent the continuation of the diffuse deformation within the Wharton basin,  
291 and both consistently ruptured orthogonal fabrics toward the top of the downgoing  
292 plate both updip and downdip from the trench, where highly oblique convergence in-  
293 herently causes a rotated state of the stress in the slab. In contrast, the 2021 East Cape  
294 earthquake, which occurred deeper beneath the top of the slab, does not align with  
295 the expected oceanic fabric, and is not obviously part of a wider, plate-scale, defor-  
296 mation field, where there is no obvious oblique convergence nor are fracture zones  
297 of an orientation consistent with the observed mechanisms subducted (Fig. 1). Instead,

298 the rupture processes may represent a unique case, highlighting a different type of  
299 stress transition within the subducted slab.

## 300 **5 A contorted slab structure due to slab buoyancy variations?**

301 A key question is why does this part of the Hikurangi subduction zone exhibit  
302 an atypical stress regime, as manifested in the rupture process of the 2021 East Cape  
303 earthquake? Slab models of this region (Hayes, 2018; Hayes et al., 2018; Williams et  
304 al., 2013) show a homogeneous planar structure (Fig. S9) which would be expected  
305 to lead to a trench-normal compression in the deeper part of the slab. However, these  
306 slab models are poorly constrained near the East Cape earthquake, largely because of  
307 a lack of plate interface thrust earthquakes in the region (Fig. 1). The rupture pro-  
308 cess of the East Cape earthquake therefore potentially offers new insight into the lo-  
309 cal slab structure.

310 One possible explanation is that the slab surface warps downward north of the  
311 hypocenter, forming a depression at the plate interface (Fig. 4). The warping is likely  
312 a response to the buoyancy gradients in the subducting plate, which allows the less  
313 buoyant parts of the slab to sink more rapidly than the buoyant parts. The internal  
314 stress field from such a slab topology would be complex, leading to strong 3-D stress  
315 rotations around the localized downwarp in a manner as shown in the 2021 East Cape  
316 earthquake (Fig. 2). One contribution to the buoyancy gradients might be the sub-  
317 duction of a large-scale seamount. About 30 km south-west from the epicenter, the  
318 Quaternary Ruatoria seamount was obliquely subducted at the margin (Lewis et al.,  
319 1998; Collot et al., 2001; Lewis et al., 2004), forming the characteristic bathymetry of  
320 the Ruatoria indentation (Fig. 1). The Ruatoria seamount could deflect and bend the  
321 slab, causing the intraslab stress state to rotate from trench-normal compression to  
322 trench-parallel compression across the hypocentral area. Numerical models of slab  
323 stress in the presence of subducted buoyant features in the oceanic plate support such  
324 a stress rotation and lateral spreading mechanism (e.g., Mason et al., 2010).

325 An alternative explanation may arise from the location of the East Cape earth-  
326 quake with respect to the transition between the Kermadec trench and Hikurangi mar-  
327 gin, marked by the edge of the Hikurangi plateau, which is represented by a clear bathy-  
328 metric scarp running along its northern boundary (Davy & Collot, 2000). This tran-  
329 sition from the subduction of normal oceanic lithosphere to the north, to the subduc-  
330 tion of the thickened oceanic crust associated with the igneous Hikurangi plateau likely  
331 leads to a pronounced, short-wavelength flexural warping at the plateaus edge. The  
332 superposition of this N-S flexural stress field with the stress field related to the down-

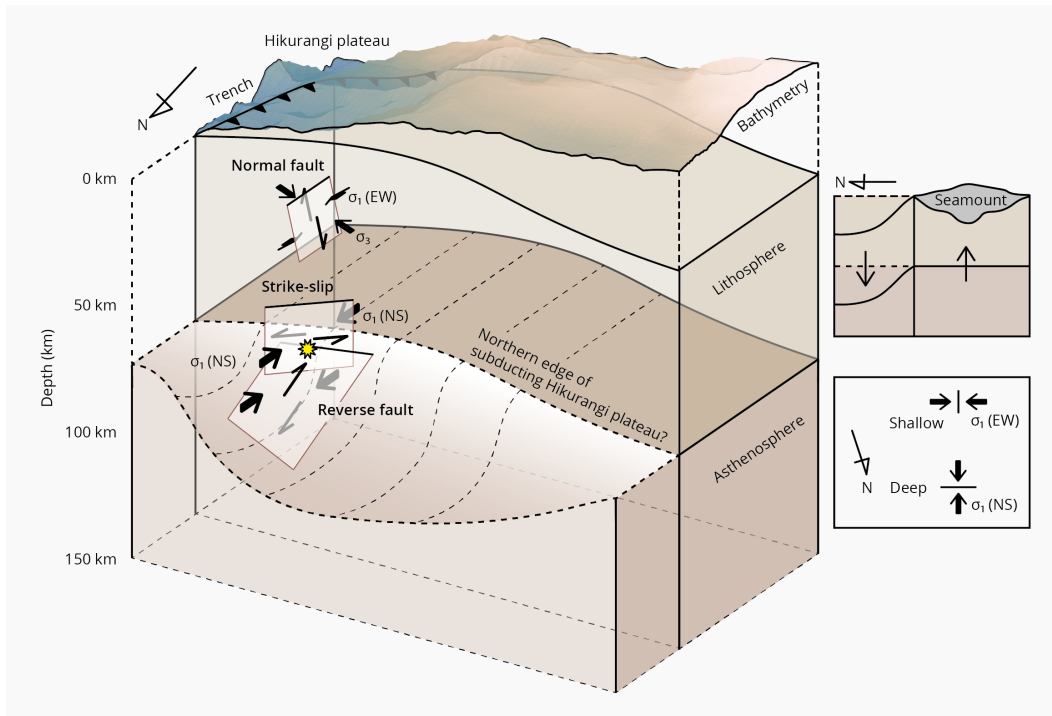


**Figure 4.** Schematic figure showing the inferred slab geometry, stress regimes and faulting styles based on our observations of the 2021 East Cape earthquake. The yellow marker shows the hypocenter. The arrow shows the stress orientations. The one-side arrow represents the fault motion. The bathymetry is from Mitchell et al. (2012) with its height being exaggerated  $\times 15$ . The upper right panel is a cross-section with the arrows showing the relative force applied in the slab. The lower right panel shows the expected principal stress ( $\sigma_1$ ) orientations in a top view.

333 dip bending would produce a complex pattern that varies at short-length scales within  
 334 the subducted slab, and could impact on the rupture process seen in the compound  
 335 East Cape earthquake.

336 Whilst there have been many studies on the impact of subducting buoyant fea-  
 337 tures on subduction megathrust coupling and interface seismogenesis (e.g., Wang &  
 338 Bilek, 2011; Nishikawa & Ide, 2014), there have been far fewer studies that have con-  
 339 sidered their impact on intraslab seismicity. The rarity of deep intraslab earthquakes  
 340 in the northern Hikurangi subduction zone makes it difficult to distinguish between  
 341 the seamount and plateau models of stress rotation. However, it is also possible that  
 342 both features play a concurrent role, with stress rotations superimposed from both.

343

## 344 6 Conclusions

345 We determined the rupture geometry of the 2021  $M_W$  7.3 East Cape, New Zealand  
346 earthquake using a novel finite-fault inversion technique. Our method does not re-  
347 quire a-priori knowledge of the fault geometry and can flexibly resolve complex fault-  
348 ing styles in large earthquakes. Therefore, it can uniquely illuminate the heterogeneous  
349 stress state near the earthquake. We show that the East Cape earthquake has at least  
350 four rupture episodes and likely ruptured multiple faults with various faulting styles.  
351 We find distinct rupture episodes within the shallow ( $\sim 30$  km) and deep ( $\sim 70$  km)  
352 parts of the subducted oceanic plate, with distinct mechanisms of normal and a mix-  
353 ture of strike-slip and reverse faulting, respectively. The deep and shallow episodes  
354 likely reflect components of a flexural stress field, separated by a low-stress barrier  
355 in the middle of the plate. The rotation of P-axes suggests that the intraplate stress  
356 state is locally rotated from trench-normal compression to trench-parallel compres-  
357 sion. Such a stress rotation in depth requires the slab geometry to change sharply, which  
358 may have been induced by a subducted seamount or the additional buoyancy of the  
359 Hikurangi plateau. Our study suggests that understanding the generation of interme-  
360 diate and deep intraslab seismicity requires a detailed treatment of localized varia-  
361 tions in slab geometry caused by the subduction of heterogeneous features, such as  
362 ocean plateaus and seamounts.

## 363 **Acknowledgments**

364 We thank the editor and the reviewers for their evaluations. We thank Lingsen Meng,  
365 Han Bao, Baoning Wu, Richard G. Davy, Lior Suchoy, Fangqin Chen, Rhodri Davies,  
366 Tian Feng, Yuqing Xie, Liuwei Xu and Tong Zhou for the discussions. We are also grate-  
367 ful to John Ristau for discussions on the original GeoNet moment tensor solutions.  
368 TJC was supported in this work by the Royal Society under URF\R1\180088. COMET  
369 is the NERC Centre for the Observation and Modelling of Earthquakes, Volcanoes and  
370 Tectonics, a partnership between UK Universities and the British Geological Survey.  
371 This work was supported by the Grant-in-Aid for Scientific Research (C) 19K04030.  
372 The facilities of IRIS Data Services, and specifically the IRIS Data Management Cen-  
373 ter, were used for access to waveforms, related metadata, and/or derived products used  
374 in this study. IRIS Data Services are funded through the Seismological Facilities for  
375 the Advancement of Geoscience (SAGE) Award of the National Science Foundation  
376 under Cooperative Support Agreement EAR-1851048. We also thank the GeoNet data  
377 centre for making their continuous broadband and strong motion seismic data openly  
378 available. The authors declare no conflicts of interest relevant to this study.

## 379 **Data Availability Statement**

380 All the materials presented in this paper are archived and available at [https://doi.org/](https://doi.org/10.5281/zenodo.5068091)  
381 [10.5281/zenodo.5068091](https://doi.org/10.5281/zenodo.5068091). All seismic data were downloaded through the IRIS Wilber  
382 3 system ([https://ds.iris.edu/wilber3/find\\_event](https://ds.iris.edu/wilber3/find_event)) or IRIS Web Services ([https://service](https://service.iris.edu)  
383 [.iris.edu](https://service.iris.edu)), including the following seismic networks: the GT (Global Telemetered Seis-  
384 mograph Network (USAF/USGS); Albuquerque Seismological Laboratory (ASL)/USGS,  
385 1993); the IC (New China Digital Seismograph Network; Albuquerque Seismological  
386 Laboratory (ASL)/USGS, 1992); the IU (Global Seismograph Network (GSN - IRIS/USGS);  
387 Albuquerque Seismological Laboratory (ASL)/USGS, 1988); the GE (GEOFON Seis-  
388 mic Network; GEOFON Data Centre, 1993); the AU (Australian National Seismograph  
389 Network (ANSN); Geoscience Australia (GA), 1994); the HK (Hong Kong Seismograph  
390 Network; Hong Kong Observatory, 2009); the G (GEOSCOPE; Institut De Physique  
391 Du Globe De Paris (IPGP) & Ecole Et Observatoire Des Sciences De La Terre De Stras-  
392 bourg (EOST), 1982); the NZ (New Zealand National Seismograph Network; Institute  
393 of Geological & Nuclear Sciences Ltd (GNS New Zealand), 1988; Petersen et al., 2011);  
394 the AI (Antarctic Seismographic Argentinean Italian Network - OGS; Istituto Nazionale  
395 Di Oceanografia E Di Geofisica Sperimentale, 1992); the II (IRIS/IDA Seismic Network;  
396 Scripps Institution Of Oceanography, 1986); the C (Chilean National Seismic Network;  
397 Universidad de Chile Dept de Geofisica (DGF UChile Chile), 1991); the PS (Pacific21



398 (ERI/STA); University of Tokyo Earthquake Research Institute (Todai ERI Japan), 1989).  
 399 We used ObsPy (Beyreuther et al., 2010, version 1.1.0; [https://doi.org/10.5281/zenodo](https://doi.org/10.5281/zenodo.165135)  
 400 [.165135](https://doi.org/10.5281/zenodo.165135)), Pyrocko (The Pyrocko Developers, 2017, <https://pyrocko.org/>), matplotlib  
 401 (Hunter, 2007, version 3.0.3; <https://doi.org/10.5281/zenodo.2577644>), Generic Map-  
 402 ping Tools (Wessel & Luis, 2017, version 6.1.0; <http://doi.org/10.5281/zenodo.3924517>);  
 403 and Scientific colour maps (Cramer et al., 2018; Cramer et al., 2020, version 6.0.4; [http://](http://doi.org/10.5281/zenodo.4153113)  
 404 [doi.org/10.5281/zenodo.4153113](http://doi.org/10.5281/zenodo.4153113)) for data processing and visualisation. The NonLin-  
 405 Loc software used for hypocenter relocation is available at <http://alomax.free.fr/nlloc/>.  
 406 The Grond software (Heimann et al., 2018) used for *W*-phase CMT inversion is avail-  
 407 able at <https://pyrocko.org/grond/docs/current/>. The ISOLA software used for R-CMT  
 408 inversion is available at <http://seismo.geology.upatras.gr/isola/>. The COMLOC earth-  
 409 quake location package (Lin & Shearer, 2005, 2006) for aftershock relocation is avail-  
 410 able at <https://sites.google.com/view/guoqing-lin/products/complc>.

## 411 References

- 412 Abercrombie, R. E., Antolik, M., & Ekström, G. (2003). The June 2000 Mw 7.9  
 413 earthquakes south of Sumatra: Deformation in the India-Australia Plate. *J.*  
 414 *Geophys. Res. Solid Earth*, 108(B1), 2003. doi:10.1029/2001jb000674
- 415 Aki, K. (1979). Characterization of barriers on an earthquake fault. *J. Geophys. Res.*,  
 416 84(B11), 6140. doi:10.1029/JB084iB11p06140
- 417 Albuquerque Seismological Laboratory (ASL)/USGS. (1988). *Global Seismograph*  
 418 *Network (GSN - IRIS/USGS)*. International Federation of Digital Seismograph  
 419 Networks. doi:10.7914/SN/IU
- 420 Albuquerque Seismological Laboratory (ASL)/USGS. (1992). *New China Digital Seis-*  
 421 *mograph Network*. International Federation of Digital Seismograph Networks.  
 422 doi:10.7914/SN/IC
- 423 Albuquerque Seismological Laboratory (ASL)/USGS. (1993). *Global Telemetered*  
 424 *Seismograph Network (USAF/USGS)*. International Federation of Digital Seis-  
 425 mograph Networks. Retrieved from [http://www.fdsn.org/doi/10.7914/SN/](http://www.fdsn.org/doi/10.7914/SN/GT)  
 426 [GT](http://www.fdsn.org/doi/10.7914/SN/GT) doi:10.7914/SN/GT
- 427 Ammon, C. J., Kanamori, H., & Lay, T. (2008). A great earthquake doublet and seis-  
 428 mic stress transfer cycle in the central Kuril islands. *Nature*, 451(7178), 561–  
 429 565. doi:10.1038/nature06521
- 430 Ampuero, J.-P., & Dahlen, F. A. (2005). Ambiguity of the Moment Tensor. *Bull. Seis-*  
 431 *mol. Soc. Am.*, 95(2), 390–400. doi:10.1785/0120040103
- 432 Arai, R., Takahashi, T., Kodaira, S., Kaiho, Y., Nakanishi, A., Fujie, G., ... Kaneda, Y.  
 433 (2016). Structure of the tsunamigenic plate boundary and low-frequency

- 434 earthquakes in the southern Ryukyu Trench. *Nat. Commun.*, 7, 1–7.  
 435 doi:10.1038/ncomms12255
- 436 Astiz, L., Lay, T., & Kanamori, H. (1988). Large intermediate-depth earthquakes  
 437 and the subduction process. *Phys. Earth Planet. Inter.*, 53(1-2), 80–166.  
 438 doi:10.1016/0031-9201(88)90138-0
- 439 Avouac, J. P., Ayoub, F., Wei, S., Ampuero, J. P., Meng, L., Leprince, S., ... Helm-  
 440 berger, D. (2014). The 2013, Mw 7.7 Balochistan earthquake, energetic  
 441 strike-slip reactivation of a thrust fault. *Earth Planet. Sci. Lett.*, 391, 128–134.  
 442 doi:10.1016/j.epsl.2014.01.036
- 443 Bassett, D., Kopp, H., Sutherland, R., Henrys, S., Watts, A. B., Timm, C., ... Ronde,  
 444 C. E. J. (2016). Crustal structure of the Kermadec arc from MANGO seis-  
 445 mic refraction profiles. *J. Geophys. Res. Solid Earth*, 121(10), 7514–7546.  
 446 doi:10.1002/2016JB013194
- 447 Bassett, D., Sutherland, R., Henrys, S., Stern, T., Scherwath, M., Benson, A., ... Hen-  
 448 derson, M. (2010). Three-dimensional velocity structure of the northern  
 449 Hikurangi margin, Raukumara, New Zealand: Implications for the growth of  
 450 continental crust by subduction erosion and tectonic underplating. *Geochem-*  
 451 *istry, Geophys. Geosystems*, 11(10). doi:10.1029/2010GC003137
- 452 Bell, R., Sutherland, R., Barker, D. H., Henrys, S., Bannister, S., Wallace, L., & Bea-  
 453 van, J. (2010). Seismic reflection character of the Hikurangi subduction  
 454 interface, New Zealand, in the region of repeated Gisborne slow slip events.  
 455 *Geophys. J. Int.*, 180(1), 34–48. doi:10.1111/j.1365-246X.2009.04401.x
- 456 Beyreuther, M., Barsch, R., Krischer, L., Megies, T., Behr, Y., & Wassermann, J.  
 457 (2010). ObsPy: A Python Toolbox for Seismology. *Seismol. Res. Lett.*, 81(3),  
 458 530–533. doi:10.1785/gssrl.81.3.530
- 459 Bird, P. (2003). An updated digital model of plate boundaries. *Geochemistry, Geo-*  
 460 *phys. Geosystems*, 4(3), 1105. doi:10.1029/2001GC000252
- 461 Collot, J. Y., Delteil, J., Lewis, K. B., Davy, B., Lamarche, G., Audru, J. C., ... Uruski,  
 462 C. (1996). From oblique subduction to intra-continental transpression:  
 463 Structures of the southern Kermadec-Hikurangi margin from multibeam  
 464 bathymetry, side-scan sonar and seismic reflection. *Mar. Geophys. Res.*, 18(2-4),  
 465 357–381. doi:10.1007/BF00286085
- 466 Collot, J. Y., Lewis, K., Lamarche, G., & Lallemand, S. (2001). The giant Ruatoria  
 467 debris avalanche on the northern Hikurangi margin, New Zealand: Result of  
 468 oblique seamount subduction. *J. Geophys. Res. Solid Earth*, 106(B9), 19271–  
 469 19297. doi:10.1029/2001jb900004
- 470 Craig, T. J., Copley, A., & Jackson, J. (2014). A reassessment of outer-rise seismicity

- 471 and its implications for the mechanics of oceanic lithosphere. *Geophys. J. Int.*,  
 472 197(1), 63–89. doi:10.1093/gji/ggu013
- 473 Cramer, F. (2018). Geodynamic diagnostics, scientific visualisation and StagLab  
 474 3.0. *Geosci. Model Dev.*, 11(6), 2541–2562. doi:10.5194/gmd-11-2541-2018
- 475 Cramer, F., Shephard, G. E., & Heron, P. J. (2020). The misuse of colour in science  
 476 communication. *Nat. Commun.*, 11(1), 5444. doi:10.1038/s41467-020-19160-  
 477 7
- 478 Das, S., & Aki, K. (1977). Fault plane with barriers: A versatile earthquake model. *J.*  
 479 *Geophys. Res.*, 82(36), 5658–5670. doi:10.1029/JB082i036p05658
- 480 Dascher-Cousineau, K., Brodsky, E. E., Lay, T., & Goebel, T. H. W. (2020). What Con-  
 481 trols Variations in Aftershock Productivity? *J. Geophys. Res. Solid Earth*, 125(2),  
 482 e2019JB018111. doi:10.1029/2019JB018111
- 483 Davey, F. J., Henrys, S., & Lodolo, E. (1997). A seismic crustal section across the East  
 484 Cape convergent margin, New Zealand. *Tectonophysics*, 269(3-4), 199–215.  
 485 doi:10.1016/S0040-1951(96)00165-5
- 486 Davy, B., & Collot, J. Y. (2000). The Rapuhia Scarp (northern Hikurangi Plateau)  
 487 - Its nature and subduction effects on the Kermadec Trench. *Tectonophysics*,  
 488 328(3-4), 269–295. doi:10.1016/S0040-1951(00)00211-0
- 489 DeMets, C., Gordon, R. G., & Argus, D. F. (2010). Geologically current plate mo-  
 490 tions. *Geophys. J. Int.*, 181(1), 1–80. doi:10.1111/j.1365-246X.2009.04491.x
- 491 Duputel, Z., Rivera, L., Kanamori, H., & Hayes, G. (2012). W phase source inversion  
 492 for moderate to large earthquakes (1990-2010). *Geophys. J. Int.*, 189(2), 1125–  
 493 1147. doi:10.1111/j.1365-246X.2012.05419.x
- 494 Dziewonski, A. M., Chou, T.-A., & Woodhouse, J. H. (1981). Determination of  
 495 earthquake source parameters from waveform data for studies of global  
 496 and regional seismicity. *J. Geophys. Res. Solid Earth*, 86(B4), 2825–2852.  
 497 doi:10.1029/JB086iB04p02825
- 498 Eberhart-Phillips, D., Bannister, S., Reyners, M., & Henrys, S. (2020). *New Zealand*  
 499 *Wide model 2.2 seismic velocity and Qs and Qp models for New Zealand*. Zenodo.  
 500 doi:10.5281/zenodo.3779523
- 501 Eberhart-Phillips, D., Reyners, M., Bannister, S., Chadwick, M., & Ellis, S. (2010).  
 502 Establishing a versatile 3-D seismic velocity model for New Zealand. *Seismol.*  
 503 *Res. Lett.*, 81(6), 992–1000. doi:10.1785/gssrl.81.6.992
- 504 Ekström, G., Nettles, M., & Dziewoński, A. (2012). The global CMT project  
 505 2004–2010: Centroid-moment tensors for 13,017 earthquakes. *Phys. Earth*  
 506 *Planet. Inter.*, 200-201, 1–9. doi:10.1016/j.pepi.2012.04.002
- 507 Elliott, J. R., Jolivet, R., Gonzalez, P. J., Avouac, J. P., Hollingsworth, J., Searle, M. P.,

- 508 & Stevens, V. L. (2016). Himalayan megathrust geometry and relation to  
 509 topography revealed by the Gorkha earthquake. *Nat. Geosci.*, 9(2), 174–180.  
 510 doi:10.1038/ngeo2623
- 511 Fischer, A. D., Peng, Z., & Sammis, C. G. (2008). Dynamic triggering of high-  
 512 frequency bursts by strong motions during the 2004 Parkfield earthquake  
 513 sequence. *Geophys. Res. Lett.*, 35(12), L12305. doi:10.1029/2008GL033905
- 514 Fischer, A. D., Sammis, C. G., Chen, Y., & Teng, T.-L. (2008). Dynamic  
 515 Triggering by Strong-Motion P and S Waves: Evidence from the 1999  
 516 Chi-Chi, Taiwan, Earthquake. *Bull. Seismol. Soc. Am.*, 98(2), 580–592.  
 517 doi:10.1785/0120070155
- 518 Floyd, M. A., Walters, R. J., Elliott, J. R., Funning, G. J., Svarc, J. L., Murray, J. R., ...  
 519 Wright, T. J. (2016). Spatial variations in fault friction related to lithology  
 520 from rupture and afterslip of the 2014 South Napa, California, earthquake.  
 521 *Geophys. Res. Lett.*, 43(13), 6808–6816. doi:10.1002/2016GL069428
- 522 GEOFON Data Centre. (1993). *GEOFON Seismic Network*. Deutsches Geo-  
 523 ForschungsZentrum GFZ. doi:10.14470/TR560404
- 524 GeoNet. (2021). *GeoNet Earthquake Catalog*. Retrieved from [https://www.geonet.org](https://www.geonet.org.nz/data/types/eq_catalogue)  
 525 [.nz/data/types/eq\\_catalogue](https://www.geonet.org.nz/data/types/eq_catalogue)
- 526 GeoNet Moment Tensors. (2021). *GeoNet Moment Tensors*. Retrieved from [https://](https://github.com/GeoNet/data/tree/main/moment-tensor)  
 527 [github.com/GeoNet/data/tree/main/moment-tensor](https://github.com/GeoNet/data/tree/main/moment-tensor)
- 528 GeoNet News. (2021). *Friday 5 March Tsunami: What happened and*  
 529 *what did you see?* Retrieved from [https://www.geonet.org.nz/news/](https://www.geonet.org.nz/news/1gvqV0oHGIULbydSQD8W1Y)  
 530 [1gvqV0oHGIULbydSQD8W1Y](https://www.geonet.org.nz/news/1gvqV0oHGIULbydSQD8W1Y)
- 531 Geoscience Australia (GA). (1994). *Australian National Seismograph Network*  
 532 *(ANSN)*. Retrieved from <https://www.fdsn.org/networks/detail/AU/>
- 533 Gomberg, J., & Bodin, P. (2021). The Productivity of Cascadia Aftershock Se-  
 534 quences. *Bull. Seismol. Soc. Am.*, 111(3), 1–14. doi:10.1785/0120200344
- 535 Hamling, I. J., Hreinsdóttir, S., Clark, K., Elliott, J., Liang, C., Fielding, E., ... Stir-  
 536 ling, M. (2017). Complex multifault rupture during the 2016 Mw 7.8 Kaikōura  
 537 earthquake, New Zealand. *Science*, 356(6334). doi:10.1126/science.aam7194
- 538 Hayes, G. P. (2018). *Slab2 - A Comprehensive Subduction Zone Geometry Model: U.S.*  
 539 *Geological Survey data release*. doi:10.5066/F7PV6JNV
- 540 Hayes, G. P., Moore, G. L., Portner, D. E., Hearne, M., Flamme, H., Furtney, M., &  
 541 Smoczyk, G. M. (2018). Slab2, a comprehensive subduction zone geometry  
 542 model. *Science*, 362(6410), 58–61. doi:10.1126/science.aat4723
- 543 Heimann, S., Isken, M., Kühn, D., Sudhaus, H., Steinberg, A., Vasyura-Bathke,  
 544 H., ... Dahm, T. (2018). *Grond - A probabilistic earthquake source inver-*

- 545        *sion framework*. Retrieved from <http://pyrocko.org/grond/docs/current/>  
546        doi:10.5880/GFZ.2.1.2018.003
- 547        Henrys, S., Reyners, M., Pecher, I., Bannister, S., Nishimura, Y., & Maslen, G. (2006).  
548        Kinking of the subducting slab by escalator normal faulting beneath the North  
549        Island of New Zealand. *Geology*, 34(9), 777–780. doi:10.1130/G22594.1
- 550        Hicks, S. P., & Rietbrock, A. (2015). Seismic slip on an upper-plate normal fault  
551        during a large subduction megathrust rupture. *Nat. Geosci.*, 8(12), 955–960.  
552        doi:10.1038/ngeo2585
- 553        Hong Kong Observatory. (2009). *Hong Kong Seismograph Network*. Retrieved from  
554        [http://www.hko.gov.hk/gts/quake/sp\\_seismo\\_network\\_intro\\_e.htm](http://www.hko.gov.hk/gts/quake/sp_seismo_network_intro_e.htm)
- 555        Hunter, J. D. (2007). Matplotlib: A 2D Graphics Environment. *Comput. Sci. Eng.*,  
556        9(3), 90–95. doi:10.1109/MCSE.2007.55
- 557        Institut De Physique Du Globe De Paris (IPGP), & Ecole Et Observatoire Des Sci-  
558        ences De La Terre De Strasbourg (EOST). (1982). *GEOSCOPE, French Global*  
559        *Network of broad band seismic stations*. Institut de physique du globe de Paris  
560        (IPGP), Université de Paris. doi:10.18715/GEOSCOPE.G
- 561        Institute of Geological & Nuclear Sciences Ltd (GNS New Zealand). (1988). *New*  
562        *Zealand National Seismograph Network*. Retrieved from [https://www.fdsn.org/](https://www.fdsn.org/networks/detail/NZ/)  
563        [networks/detail/NZ/](https://www.fdsn.org/networks/detail/NZ/)
- 564        International Seismological Centre. (2021). *On-line Bulletin*.  
565        doi:10.31905/D808B830
- 566        Istituto Nazionale Di Oceanografia E Di Geofisica Sperimentale. (1992). *Antarctic*  
567        *Seismographic Argentinean Italian Network - OGS*. International Federation of  
568        Digital Seismograph Networks. doi:10.7914/SN/AI
- 569        Kaneko, Y., Ito, Y., Chow, B., Wallace, L. M., Tape, C., Grapenthin, R., ... Hino, R.  
570        (2019). Ultra-long Duration of Seismic Ground Motion Arising From a Thick,  
571        Low-Velocity Sedimentary Wedge. *J. Geophys. Res. Solid Earth*, 124(10), 10347–  
572        10359. doi:10.1029/2019JB017795
- 573        Kikuchi, M., & Kanamori, H. (1991). Inversion of complex body waves-  
574        III. *Bull. Seism. Soc. Am.*, 81(6), 2335–2350. Retrieved from [https://](https://pubs.geoscienceworld.org/ssa/bssa/article-abstract/81/6/2335/102472/)  
575        [pubs.geoscienceworld.org/ssa/bssa/article-abstract/81/6/2335/102472/](https://pubs.geoscienceworld.org/ssa/bssa/article-abstract/81/6/2335/102472/)  
576        Inversion-of-complex-body-waves-III
- 577        Lay, T., Duputel, Z., Ye, L., & Kanamori, H. (2013). The December 7, 2012 Japan  
578        Trench intraplate doublet (Mw 7.2, 7.1) and interactions between near-trench  
579        intraplate thrust and normal faulting. *Phys. Earth Planet. Inter.*, 220, 73–78.  
580        doi:10.1016/j.pepi.2013.04.009
- 581        Lay, T., Ye, L., Wu, Z., & Kanamori, H. (2020). Macrofracturing of Oceanic Litho-

- 582 sphere in Complex Large Earthquake Sequences. *J. Geophys. Res. Solid Earth*,  
 583 125(10), 1–21. doi:10.1029/2020JB020137
- 584 Lewis, K. B., Collot, J. Y., & Lallemand, S. E. (1998). The dammed Hikurangi  
 585 Trough: A channel-fed trench blocked by subducting seamounts and their  
 586 wake avalanches (New Zealand-France GeodyNZ Project). *Basin Res.*, 10(4),  
 587 441–468. doi:10.1046/j.1365-2117.1998.00080.x
- 588 Lewis, K. B., Lallemand, S. E., & Carter, L. (2004). Collapse in a quaternary  
 589 shelf basin off East Cape, New Zealand: Evidence for passage of a subducted  
 590 seamount inboard of the ruatoria giant avalanche. *New Zeal. J. Geol. Geophys.*,  
 591 47(3), 415–429. doi:10.1080/00288306.2004.9515067
- 592 Lin, G., & Shearer, P. (2005). Tests of relative earthquake location tech-  
 593 niques using synthetic data. *J. Geophys. Res. Solid Earth*, 110(B4), 1–14.  
 594 doi:10.1029/2004JB003380
- 595 Lin, G., & Shearer, P. (2006). The COMLOC Earthquake Location Package. *Seismol.*  
 596 *Res. Lett.*, 77(4), 440–444. doi:10.1785/gssrl.77.4.440
- 597 Mason, W. G., Moresi, L., Betts, P. G., & Miller, M. S. (2010). Three-dimensional  
 598 numerical models of the influence of a buoyant oceanic plateau on subduction  
 599 zones. *Tectonophysics*, 483(1-2), 71–79. doi:10.1016/j.tecto.2009.08.021
- 600 Meng, L., Ampuero, J. P., Stock, J., Duputel, Z., Luo, Y., & Tsai, V. C. (2012).  
 601 Earthquake in a maze: Compressional rupture branching during the  
 602 2012 Mw 8.6 Sumatra earthquake. *Science*, 337(6095), 724–726.  
 603 doi:10.1126/science.1224030
- 604 Mitchell, J. S., Mackay, K. A., Neil, H. L., Mackay, E. J., Pallentin, A., & Notman,  
 605 P. (2012). Undersea New Zealand, 1: 5,000,000. *NIWA chart, Misc. Ser.*,  
 606 92. Retrieved from [https://niwa.co.nz/our-science/oceans/bathymetry/  
 607 further-information](https://niwa.co.nz/our-science/oceans/bathymetry/further-information)
- 608 Miyazawa, M., & Mori, J. (2005). Detection of triggered deep low-frequency  
 609 events from the 2003 Tokachi-oki earthquake. *Geophys. Res. Lett.*, 32(10),  
 610 1–4. doi:10.1029/2005GL022539
- 611 Nishikawa, T., & Ide, S. (2014). Earthquake size distribution in subduction zones  
 612 linked to slab buoyancy. *Nat. Geosci.*, 7(12), 904–908. doi:10.1038/ngeo2279
- 613 Nishikawa, T., Nishimura, T., & Okada, Y. (2021). Earthquake Swarm Detection  
 614 Along the Hikurangi Trench, New Zealand: Insights Into the Relationship  
 615 Between Seismicity and Slow Slip Events. *J. Geophys. Res. Solid Earth*, 126(4),  
 616 1–31. doi:10.1029/2020JB020618
- 617 Ohta, Y., Miura, S., Ohzono, M., Kita, S., Linuma, T., Demachi, T., ... Umino, N.  
 618 (2011). Large intraslab earthquake (2011 April 7, M 7.1) after the 2011

- 619 off the Pacific coast of Tohoku Earthquake (M 9.0): Coseismic fault model  
 620 based on the dense GPS network data. *Earth, Planets Sp.*, 63(12), 1207–1211.  
 621 doi:10.5047/eps.2011.07.016
- 622 Okada, T., & Hasegawa, A. (2003). The M7.1 May 26, 2003 off-shore Miyagi  
 623 Prefecture Earthquake in northeast Japan: Source process and aftershock  
 624 distribution of an intra-slab event. *Earth, Planets Sp.*, 55(12), 731–739.  
 625 doi:10.1186/BF03352482
- 626 Okuwaki, R., Hirano, S., Yagi, Y., & Shimizu, K. (2020). Inchworm-like source  
 627 evolution through a geometrically complex fault fueled persistent supershear  
 628 rupture during the 2018 Palu Indonesia earthquake. *Earth Planet. Sci. Lett.*,  
 629 547, 116449. doi:10.1016/j.epsl.2020.116449
- 630 Page, M. T., van Der Elst, N., Hardebeck, J., Felzer, K., & Michael, A. J. (2016).  
 631 Three ingredients for improved global aftershock forecasts: Tectonic region,  
 632 time-dependent catalog incompleteness, and intersequence variability. *Bull.*  
 633 *Seismol. Soc. Am.*, 106(5), 2290–2301. doi:10.1785/0120160073
- 634 Petersen, T., Gledhill, K., Chadwick, M., Gale, N. H., & Ristau, J. (2011). The New  
 635 Zealand National Seismograph Network. *Seismol. Res. Lett.*, 82(1), 9–20.  
 636 doi:10.1785/gssrl.82.1.9
- 637 Ranero, C. R., Villaseñor, A., Morgan, J. P., & Weinrebe, W. (2005). Relationship be-  
 638 tween bend-faulting at trenches and intermediate-depth seismicity. *Geochem-*  
 639 *istry, Geophys. Geosystems*, 6(12). doi:10.1029/2005GC000997
- 640 Reyners, M., & McGinty, P. (1999). Shallow subduction tectonics in the Raukumara  
 641 Peninsula, New Zealand, as illuminated by earthquake focal mechanisms. *J.*  
 642 *Geophys. Res. Solid Earth*, 104(B2), 3025–3034. doi:10.1029/1998JB900081
- 643 Richards-Dinger, K. B., & Shearer, P. M. (2000). Earthquake locations in southern  
 644 California obtained using source-specific station terms. *J. Geophys. Res. Solid*  
 645 *Earth*, 105(B5), 10939–10960. doi:10.1029/2000JB900014
- 646 Romeo, I., & Álvarez-Gómez, J. A. (2018). Lithospheric folding by flexural slip in  
 647 subduction zones as source for reverse fault intraslab earthquakes. *Sci. Rep.*,  
 648 8(1), 1–9. doi:10.1038/s41598-018-19682-7
- 649 Sandiford, D., Moresi, L., Sandiford, M., & Yang, T. (2019). Geometric  
 650 controls on flat slab seismicity. *Earth Planet. Sci. Lett.*, 527, 115787.  
 651 doi:10.1016/j.epsl.2019.115787
- 652 Sandiford, D., Moresi, L. M., Sandiford, M., Farrington, R., & Yang, T. (2020).  
 653 The Fingerprints of Flexure in Slab Seismicity. *Tectonics*, 39(8).  
 654 doi:10.1029/2019TC005894
- 655 Scripps Institution Of Oceanography. (1986). *IRIS/IDA Seismic Network*. Interna-

- 656 tional Federation of Digital Seismograph Networks. doi:10.7914/SN/II
- 657 Shimizu, K., Yagi, Y., Okuwaki, R., & Fukahata, Y. (2020). Development of an inver-  
658 sion method to extract information on fault geometry from teleseismic data.  
659 *Geophys. J. Int.*, 220(2), 1055–1065. doi:10.1093/gji/ggz496
- 660 Shimizu, K., Yagi, Y., Okuwaki, R., & Fukahata, Y. (2021). Construction of fault  
661 geometry by finite-fault inversion of teleseismic data. *Geophys. J. Int.*, 224(2),  
662 1003–1014. doi:10.1093/gji/ggaa501
- 663 Simons, M., Fialko, Y., & Rivera, L. (2002). Coseismic deformation from the  
664 1999 Mw 7.1 Hector Mine, California, earthquake as inferred from In-  
665 SAR and GPS observations. *Bull. Seismol. Soc. Am.*, 92(4), 1390–1402.  
666 doi:10.1785/0120000933
- 667 Sippl, C., Schurr, B., Asch, G., & Kummerow, J. (2018). Seismicity Struc-  
668 ture of the Northern Chile Forearc From >100,000 Double-Difference  
669 Relocated Hypocenters. *J. Geophys. Res. Solid Earth*, 123(5), 4063–4087.  
670 doi:10.1002/2017JB015384
- 671 Sleep, N. H., & Ma, S. (2008). Production of brief extreme ground acceleration  
672 pulses by nonlinear mechanisms in the shallow subsurface. *Geochemistry, Geo-*  
673 *phys. Geosystems*, 9(3), Q03008. doi:10.1029/2007GC001863
- 674 Tadapansawut, T., Okuwaki, R., Yagi, Y., & Yamashita, S. (2021). Rupture Process of  
675 the 2020 Caribbean Earthquake Along the Oriente Transform Fault, Involving  
676 Supershear Rupture and Geometric Complexity of Fault. *Geophys. Res. Lett.*,  
677 48(1), 1–9. doi:10.1029/2020GL090899
- 678 Tanioka, Y., Ruff, L., & Satake, K. (1995). The great Kurile Earthquake of  
679 October 4, 1994 tore the slab. *Geophys. Res. Lett.*, 22(13), 1661–1664.  
680 doi:10.1029/95GL01656
- 681 The Pyrocko Developers. (2017). *Pyrocko: A Versatile Seismology Toolkit for Python*.  
682 Retrieved from <http://pyrocko.org> doi:10.5880/GFZ.2.1.2017.001
- 683 Todd, E. K., & Lay, T. (2013). The 2011 Northern Kermadec earthquake doublet and  
684 subduction zone faulting interactions. *J. Geophys. Res. Solid Earth*, 118(1), 249–  
685 261. doi:10.1029/2012JB009711
- 686 Universidad de Chile Dept de Geofisica (DGF UChile Chile). (1991). *Chilean Na-*  
687 *tional Seismic Network*. Retrieved from [https://www.fdsn.org/networks/](https://www.fdsn.org/networks/detail/C/)  
688 [detail/C/](https://www.fdsn.org/networks/detail/C/)
- 689 University of Tokyo Earthquake Research Institute (Todai ERI Japan). (1989). *Pa-*  
690 *cific21 (ERI/STA)*. Retrieved from [https://www.fdsn.org/networks/detail/](https://www.fdsn.org/networks/detail/PS/)  
691 [PS/](https://www.fdsn.org/networks/detail/PS/)
- 692 U.S. Geological Survey Earthquake Hazards Program. (2017). *Advanced National*



- 693        *Seismic System (ANSS) Comprehensive Catalog of Earthquake Events and Prod-*  
694        *ucts.* doi:10.5066/F7MS3QZH
- 695        Wallace, L. M., Reyners, M., Cochran, U., Bannister, S., Barnes, P. M., Berryman, K.,  
696        ... Power, W. (2009). Characterizing the seismogenic zone of a major plate  
697        boundary subduction thrust: Hikurangi Margin, New Zealand. *Geochemistry,*  
698        *Geophys. Geosystems*, 10(10). doi:10.1029/2009GC002610
- 699        Wang, K., & Bilek, S. L. (2011). Do subducting seamounts generate or stop large  
700        earthquakes? *Geology*, 39(9), 819–822. doi:10.1130/G31856.1
- 701        Wessel, P., & Luis, J. F. (2017). The GMT/MATLAB Toolbox. *Geochemistry, Geophys.*  
702        *Geosystems*, 18(2), 811–823. doi:10.1002/2016GC006723
- 703        Wiens, D. A. (2001). Seismological constraints on the mechanism of deep earth-  
704        quakes: Temperature dependence of deep earthquake source properties. *Phys.*  
705        *Earth Planet. Inter.*, 127(1-4), 145–163. doi:10.1016/S0031-9201(01)00225-4
- 706        Williams, C. A., Eberhart-Phillips, D., Bannister, S., Barker, D. H., Henrys, S., Reyn-  
707        ers, M., & Sutherland, R. (2013). Revised interface geometry for the hiku-  
708        rangi subduction zone, New Zealand. *Seismol. Res. Lett.*, 84(6), 1066–1073.  
709        doi:10.1785/0220130035
- 710        Wiseman, K., Banerjee, P., Bürgmann, R., Sieh, K., Dreger, D. S., & Hermawan,  
711        I. (2012). Source model of the 2009 Mw 7.6 Padang intraslab earthquake  
712        and its effect on the Sunda megathrust. *Geophys. J. Int.*, 190(3), 1710–1722.  
713        doi:10.1111/j.1365-246X.2012.05600.x
- 714        Yamashita, S., Yagi, Y., Okuwaki, R., Shimizu, K., Agata, R., & Fukahata, Y. (2021).  
715        Consecutive ruptures on a complex conjugate fault system during the 2018  
716        Gulf of Alaska earthquake. *Sci. Rep.*, 11(1), 5979. doi:10.1038/s41598-021-  
717        85522-w
- 718        Ye, L., Lay, T., Bai, Y., Cheung, K. F., & Kanamori, H. (2017). The 2017 Mw 8.2  
719        Chiapas, Mexico, Earthquake: Energetic Slab Detachment. *Geophys. Res. Lett.*,  
720        44(23), 11,824–11,832. doi:10.1002/2017GL076085
- 721        Ye, L., Lay, T., & Kanamori, H. (2012). Intraplate and interplate faulting interactions  
722        during the August 31, 2012, Philippine Trench earthquake (Mw 7.6) sequence.  
723        *Geophys. Res. Lett.*, 39(24), 1–6. doi:10.1029/2012GL054164
- 724        Ye, L., Lay, T., & Kanamori, H. (2021). The 25 March 2020 Mw 7.5 Paramushir,  
725        northern Kuril Islands earthquake and major (Mw $\geq$ 7.0) near-trench intraplate  
726        compressional faulting. *Earth Planet. Sci. Lett.*, 556(March 2020), 116728.  
727        doi:10.1016/j.epsl.2020.116728
- 728        Yue, H., Lay, T., & Koper, K. D. (2012). En échelon and orthogonal fault ruptures  
729        of the 11 April 2012 great intraplate earthquakes. *Nature*, 490(7419), 245–249.

730 doi:10.1038/nature11492

731 **References From the Supporting Information**

- 732 Ampuero, J.-P., & Dahlen, F. A. (2005). Ambiguity of the Moment Tensor. *Bull. Seis-*  
 733 *mol. Soc. Am.*, 95(2), 390–400. doi:10.1785/0120040103
- 734 Bird, P. (2003). An updated digital model of plate boundaries. *Geochemistry, Geo-*  
 735 *phys. Geosystems*, 4(3), 1105. doi:10.1029/2001GC000252
- 736 Bormann, P. (2012). New Manual of Seismological Observatory Practice (NMSOP-2).  
 737 *IASPEI, GFZ Ger. Res. Cent. Geosci.*. doi:10.2312/GFZ.NMSOP-2
- 738 Duputel, Z., Rivera, L., Kanamori, H., & Hayes, G. (2012). W phase source inversion  
 739 for moderate to large earthquakes (1990-2010). *Geophys. J. Int.*, 189(2), 1125–  
 740 1147. doi:10.1111/j.1365-246X.2012.05419.x
- 741 Dziewonski, A. M., Chou, T.-A., & Woodhouse, J. H. (1981). Determination of  
 742 earthquake source parameters from waveform data for studies of global  
 743 and regional seismicity. *J. Geophys. Res. Solid Earth*, 86(B4), 2825–2852.  
 744 doi:10.1029/JB086iB04p02825
- 745 Eberhart-Phillips, D., Bannister, S., Reyners, M., & Henrys, S. (2020). *New Zealand*  
 746 *Wide model 2.2 seismic velocity and Qs and Qp models for New Zealand*. Zenodo.  
 747 doi:10.5281/zenodo.3779523
- 748 Eberhart-Phillips, D., Reyners, M., Bannister, S., Chadwick, M., & Ellis, S. (2010).  
 749 Establishing a versatile 3-D seismic velocity model for New Zealand. *Seismol.*  
 750 *Res. Lett.*, 81(6), 992–1000. doi:10.1785/gssrl.81.6.992
- 751 Ekström, G., Nettles, M., & Dziewoński, A. (2012). The global CMT project  
 752 2004–2010: Centroid-moment tensors for 13,017 earthquakes. *Phys. Earth*  
 753 *Planet. Inter.*, 200-201, 1–9. doi:10.1016/j.pepi.2012.04.002
- 754 GeoNet. (2021). *GeoNet Earthquake Catalog*. Retrieved from [https://www.geonet.org](https://www.geonet.org.nz/data/types/eq_catalogue)  
 755 [.nz/data/types/eq\\_catalogue](https://www.geonet.org.nz/data/types/eq_catalogue)
- 756 GeoNet Moment Tensors. (2021). *GeoNet Moment Tensors*. Retrieved from [https://](https://github.com/GeoNet/data/tree/main/moment-tensor)  
 757 [github.com/GeoNet/data/tree/main/moment-tensor](https://github.com/GeoNet/data/tree/main/moment-tensor)
- 758 Hayes, G. P. (2018). *Slab2 - A Comprehensive Subduction Zone Geometry Model: U.S.*  
 759 *Geological Survey data release*. doi:10.5066/F7PV6JNV
- 760 Hayes, G. P., Moore, G. L., Portner, D. E., Hearne, M., Flamme, H., Furtney, M., &  
 761 Smoczyk, G. M. (2018). Slab2, a comprehensive subduction zone geometry  
 762 model. *Science*, 362(6410), 58–61. doi:10.1126/science.aat4723
- 763 Heimann, S., Isken, M., Kühn, D., Sudhaus, H., Steinberg, A., Vasyura-Bathke,  
 764 H., ... Dahm, T. (2018). *Grond - A probabilistic earthquake source inver-*  
 765 *sion framework*. Retrieved from <http://pyrocko.org/grond/docs/current/>

- 766 doi:10.5880/GFZ.2.1.2018.003
- 767 Kennett, B. L., Engdahl, E. R., & Buland, R. (1995). Constraints on seismic ve-  
 768 locities in the Earth from traveltimes. *Geophys. J. Int.*, 122(1), 108–124.  
 769 doi:10.1111/j.1365-246X.1995.tb03540.x
- 770 Kikuchi, M., & Kanamori, H. (1991). Inversion of complex body waves-  
 771 III. *Bull. Seism. Soc. Am.*, 81(6), 2335–2350. Retrieved from [https://](https://pubs.geoscienceworld.org/ssa/bssa/article-abstract/81/6/2335/102472/)  
 772 [pubs.geoscienceworld.org/ssa/bssa/article-abstract/81/6/2335/102472/](https://pubs.geoscienceworld.org/ssa/bssa/article-abstract/81/6/2335/102472/)  
 773 Inversion-of-complex-body-waves-III
- 774 Laske, G., Masters, T. G., Ma, Z., & Pasyanos, M. (2013). Update on CRUST1.0  
 775 - A 1-degree Global Model of Earth's Crust. *Geophys. Res. Abstr.* 15, *Ab-*  
 776 *str. EGU2013-2658*, 15, Abstract EGU2013–2658. Retrieved from [https://](https://igppweb.ucsd.edu/~gabi/crust1.html)  
 777 [igppweb.ucsd.edu/~gabi/crust1.html](https://igppweb.ucsd.edu/~gabi/crust1.html)
- 778 Lin, G., & Shearer, P. (2005). Tests of relative earthquake location tech-  
 779 niques using synthetic data. *J. Geophys. Res. Solid Earth*, 110(B4), 1–14.  
 780 doi:10.1029/2004JB003380
- 781 Lin, G., & Shearer, P. (2006). The COMLOC Earthquake Location Package. *Seismol.*  
 782 *Res. Lett.*, 77(4), 440–444. doi:10.1785/gssrl.77.4.440
- 783 Lomax, A., Michelini, A., & Curtis, A. (2009). Earthquake Location, Direct, Global-  
 784 Search Methods BT - Encyclopedia of Complexity and Systems Science. *Encycl.*  
 785 *Complex. Syst. Sci.*, 2449–2473. doi:10.1007/978-0-387-30440-3\_150
- 786 Lomax, A., Virieux, J., Volant, P., & Berge-Thierry, C. (2000). Probabilistic Earth-  
 787 quake Location in 3D and Layered Models BT - Advances in Seismic Event  
 788 Location. In C. H. Thurber & N. Rabinowitz (Eds.), (pp. 101–134). Dordrecht:  
 789 Springer Netherlands. doi:10.1007/978-94-015-9536-0\_5
- 790 Okuwaki, R., Hirano, S., Yagi, Y., & Shimizu, K. (2020). Inchworm-like source  
 791 evolution through a geometrically complex fault fueled persistent supershear  
 792 rupture during the 2018 Palu Indonesia earthquake. *Earth Planet. Sci. Lett.*,  
 793 547, 116449. doi:10.1016/j.epsl.2020.116449
- 794 Okuwaki, R., Yagi, Y., Aránguiz, R., González, J., & González, G. (2016). Rupture  
 795 Process During the 2015 Illapel, Chile Earthquake: Zigzag-Along-Dip Rupture  
 796 Episodes. *Pure Appl. Geophys.*, 173(4), 1011–1020. doi:10.1007/s00024-016-  
 797 1271-6
- 798 Petersen, T., Gledhill, K., Chadwick, M., Gale, N. H., & Ristau, J. (2011). The New  
 799 Zealand National Seismograph Network. *Seismol. Res. Lett.*, 82(1), 9–20.  
 800 doi:10.1785/gssrl.82.1.9
- 801 Shimizu, K., Yagi, Y., Okuwaki, R., & Fukahata, Y. (2020). Development of an inver-  
 802 sion method to extract information on fault geometry from teleseismic data.

- 803           *Geophys. J. Int.*, 220(2), 1055–1065. doi:10.1093/gji/ggz496
- 804 Shimizu, K., Yagi, Y., Okuwaki, R., & Fukahata, Y. (2021). Construction of fault  
805 geometry by finite-fault inversion of teleseismic data. *Geophys. J. Int.*, 224(2),  
806 1003–1014. doi:10.1093/gji/ggaa501
- 807 Sokos, E. N., & Zahradnik, J. (2008). ISOLA a Fortran code and a Matlab GUI to per-  
808 form multiple-point source inversion of seismic data. *Comput. Geosci.*, 34(8),  
809 967–977. doi:10.1016/j.cageo.2007.07.005
- 810 Tadapansawut, T., Okuwaki, R., Yagi, Y., & Yamashita, S. (2021). Rupture Process of  
811 the 2020 Caribbean Earthquake Along the Oriente Transform Fault, Involving  
812 Supershear Rupture and Geometric Complexity of Fault. *Geophys. Res. Lett.*,  
813 48(1), 1–9. doi:10.1029/2020GL090899
- 814 U.S. Geological Survey Earthquake Hazards Program. (2017). *Advanced National*  
815 *Seismic System (ANSS) Comprehensive Catalog of Earthquake Events and Prod-*  
816 *ucts*. doi:10.5066/F7MS3QZH
- 817 Vallée, M. (2013). Source time function properties indicate a strain drop in-  
818 dependent of earthquake depth and magnitude. *Nat. Commun.*, 4, 1–6.  
819 doi:10.1038/ncomms3606
- 820 Vallée, M., Charléty, J., Ferreira, A. M., Delouis, B., & Vergoz, J. (2011). SCARDEC:  
821 A new technique for the rapid determination of seismic moment magnitude,  
822 focal mechanism and source time functions for large earthquakes using body-  
823 wave deconvolution. *Geophys. J. Int.*, 184(1), 338–358. doi:10.1111/j.1365-  
824 246X.2010.04836.x
- 825 Yagi, Y., & Fukahata, Y. (2011). Introduction of uncertainty of Green’s function into  
826 waveform inversion for seismic source processes. *Geophys. J. Int.*, 186(2), 711–  
827 720. doi:10.1111/j.1365-246X.2011.05043.x
- 828 Yamashita, S., Yagi, Y., Okuwaki, R., Shimizu, K., Agata, R., & Fukahata, Y. (2021).  
829 Consecutive ruptures on a complex conjugate fault system during the 2018  
830 Gulf of Alaska earthquake. *Sci. Rep.*, 11(1), 5979. doi:10.1038/s41598-021-  
831 85522-w
- 832 Ye, L., Lay, T., Bai, Y., Cheung, K. F., & Kanamori, H. (2017). The 2017 Mw 8.2  
833 Chiapas, Mexico, Earthquake: Energetic Slab Detachment. *Geophys. Res. Lett.*,  
834 44(23), 11,824–11,832. doi:10.1002/2017GL076085